A dynamical model for plasma confinement transitions*

Paweł Pilarczyk[1], Luis García[2], Benjamin A. Carreras[3] and Irene Llerena[4]

[1] Centro de Matemática, Universidade do Minho, Campus de Gualtar, 4710-057 Braga, Portugal

[2] Departamento de Física, Universidad Carlos III de Madrid, Avda. de la Universidad 30, 28911 Leganés, Madrid, Spain

[3] Department of Physics, University of Alaska at Fairbanks, P.O. Box 755920, Fairbanks, AK 99775-5920, U.S.A.

[4] Departament d'Àlgebra i Geometria, Facultat de Matemàtiques, Universitat de Barcelona, Gran Via de les Corts Catalanes, 585, 08007 Barcelona, Spain

Abstract. A three equation model describing the evolution of the turbulence level, averaged shear flow and sheared zonal flow is analyzed using topological properties of the asymptotic solutions. An exploration in parameter space is done identifying the attractor sets, which are fixed points and limit cycles. Then a more detailed analysis of all Morse sets is conducted using topological-combinatorial computations. This model allows the description of different types of transition to improved plasma confinement regimes.

1. Introduction

Magnetically confined plasmas may go through sudden transitions in which confinement improves and losses decrease. The first example of one of these transitions was the so-called high confinement mode [19], and many forms of transitions have been documented [3] [18] since then.

The dynamical mechanisms of these transitions are causing 1) amplification of the global shear flow [13] [5] [10] and 2) suppression of turbulence by the shearing of the flow [2]. The mechanism for the transition is then a flow shear dynamo instability that amplifies the shear flow through the Reynolds stress term. The amplified sheared flow reduces the turbulence fluctuations through the associated sheared electric field turbulence suppression effect.

† * This is an author-created, un-copyedited version of an article published in *Journal of Physics A: Mathematical and Theoretical*, Vol. 45, No. 12 (2012), 125502. IOP Publishing Ltd is not responsible for any errors or omissions in this version of the manuscript or any version derived from it. The definitive publisher-authenticated version is available online at journal's website. DOI: 10.1088/1751-8113/45/12/125502.

Starting with Ref. [11], dynamical models have been constructed that incorporate some of the basic mechanisms for these transitions. The derivation of these models is based on MHD equations and using the radial structures and parameter dependences of some typical plasma instabilities. Some of these models have been compared in detail with experiment [7] for the case of the transition leading to the formation of the plasma edge shear flow layer. In this case, the transition has similar characteristics to second order transitions.

As the understanding of the transition dynamics increases, more details and mechanisms have been included in the models [14] [4] making the dynamics of the transition more complicated. An example is the inclusion of the zonal flows [12] in the dynamical models.

The inclusion of the zonal flow in the dynamical models leads to different types of transitions, as it will be discussed in this paper. The character of the transition can be different from a second order transition. First order transitions and some forms of dithering transitions are now possible within those dynamical models. This type of transition may also be relevant in plasma experiments.

Some of the high confinement transitions show indications of hysteresis. This would support an interpretation based on a first order transition model. Dithering transitions have also been observed in the experiment, for instance the slow transition in the DIII-D device [8], and it is interesting to find out under what conditions these transitions are more likely.

In this paper, we analyze a simplified version of a dynamical transition model that includes the evolution of the turbulence level, an averaged poloidal flow and zonal flows. We explore the different types of transitions possible within this model. To this effect, we have used computational topological tools to analyze the model and to determine the number and topological properties of the attractor solutions.

The rest of the paper is organized as follows. In Section 2, we introduce the dynamical model and discuss some of its basic properties. In Section 3, a numerical search for attractors is presented for an ample range of values of the parameters. The method used to do this exploration is also discussed. In Section 4, topological-combinatorial calculations are done to support previous results. Finally, in Section 5 the conclusions are drawn from this research.

2. Dynamical model

Here, we consider a three-equation model combining the one proposed in Ref. [6] with the model from Ref. [14]. Our interest is to understand the interaction of averaged poloidal flow, zonal flows and turbulence. The equations are based on two dynamical mechanism affecting turbulence: one is the flow generation through Reynolds stress and the other is turbulence suppression by shear flow.

First we consider the turbulence fluctuations level on two–frequency region, the high frequency, which is given by $E \equiv \left\langle (\tilde{n}/n_0)^2 \right\rangle^{1/2}$, and the very low frequency associated

with the shear of zonal flows, $U' \equiv \left\langle \left(\partial V_{ZF\theta}/\partial r\right)^2 \right\rangle^{1/2}$. The angular brackets indicate poloidal and toroidal angular averaging over the proper frequency range.

The basic mechanism for the emergence of the shear flow layer is the Reynolds stress. The Reynolds stress term $\partial \left\langle \tilde{V}_r \tilde{V}_\theta \right\rangle /\partial r$ can be interpreted as a measure of the symmetry of the turbulent eddies. A sheared poloidal flow, $V' \equiv d\left\langle V_\theta \right\rangle /dr$, distorts those eddies and gives a net contribution to the Reynolds stress, such contribution increases the poloidal shear flow and drives an instability. This is a shear flow amplification mechanism. In this case both the low and high frequency fluctuations contribute to the Reynolds stress. So the Reynolds stress depends on the fluctuation levels and on the gradient of the averaged poloidal flow shear, and we model this term as

$$\frac{\partial^2 \left\langle \tilde{V}_r \tilde{V}_\theta \right\rangle}{\partial r^2} = -\alpha_3 E^2 V' - \alpha_4 U'^{\,2} V' \tag{1}$$

Here, α_3 and α_4 are constant coefficients. This leads to an equation for the evolution of the averaged poloidal flow of the form

$$\frac{dV'}{dt} = \alpha_3 E^2 V' + \alpha_4 U'^{\,2} V' - \mu V' \tag{2}$$

where μ is the flow damping term.

The gradient in large-scale flows, both the averaged and the zonal flows, shears the turbulence eddies and tends to suppress the turbulence. In many of the dynamical models used in the past, for instance [6], we have modeled this effect using a low shear flow limit. That is, the linear growth was written as $\gamma = \gamma_0 - \alpha_2 V'^{\,2}$, where γ_0 is the growth rate in the absence of shear flow and α_2 is a constant. However, for larger flows is better to model this effect using Ref. [2], that is, the turbulence suppression will now be written as

$$\gamma = \frac{\gamma_0}{1 + \alpha_2 V'^{\,2} + \alpha_2 U'^{\,2}} \tag{3}$$

Therefore, the equation for the evolution of the turbulence fluctuation level has the form

$$\frac{dE}{dt} = \frac{\gamma_0}{1 + \alpha_2 V'^{\,2} + \alpha_2 U'^{\,2}} E - \alpha_1 E^2 \tag{4}$$

where the term $\alpha_1 E^2$ gives the nonlinear saturation level of the turbulence.

In the case of the zonal flows, they are not driven linearly, but the drive is the Reynolds stress term. So in this case the Reynolds stress term and the suppression term are combined in a single term as was done in Ref. [14] and the equation of evolution of the zonal flow has the form

$$\frac{dU'}{dt} == \frac{\alpha_3 E^2 U'}{1 + \alpha_2 V'^{\,2}} + \alpha_5 E^2 V' - \mu U' \tag{5}$$

By renormalizing the time and the three variables of this model we can reduce the number of free parameters in the problem and finally have the following system of equations:

$$\frac{dE}{dt} = \left(\frac{1}{1 + V'^{\,2} + U'^{\,2}} - E \right) E \tag{6}$$

$$\frac{dV'}{dt} = \left(aE^2 + cU'^{\,2} - b\right) V' \tag{7}$$

$$\frac{dU'}{dt} = \left(\frac{aE^2}{1+V'^{\,2}} - b\right) U' + dE^2 V' \tag{8}$$

These equations are written in dimensionless form. Here, a, b, c and d are constants greater than or equal to zero. The parameter a measures the net effect of the Reynolds and Maxwell stress tensor that causes the amplification of the shear poloidal flow from turbulence fluctuations, the parameter c corresponds to the amplification of flow mechanism by the zonal flows, and the parameter d to the amplification of zonal flows by turbulence. The parameter b measures the flow damping. The first term in Eq. (6) is the turbulence drive modified by the turbulence suppression due to averaged and zonal flows.

Although in the dynamical evolution we have four parameters, when we look for asymptotic solutions, corresponding to zero time derivative, we can reduce the number of parameters to three. In what follows, we set the constant c to a fixed value and we explore the possible asymptotic solutions for a range of values of the other three parameters.

This model has several fixed points. In general, we cannot solve analytically the fixed-point equations. We can do it for the particular case of $d = 0$. In this case, there are four types of fixed-point solutions:

1) The trivial fixed point

$$E = V' = U' = 0 \tag{9}$$

2) The low confinement fixed point

$$E = 1, \quad V' = U' = 0 \tag{10}$$

3) The high confinement fixed points with non-zero averaged shear flow, when $b < a$,

$$E = \sqrt{\frac{b}{a}}, \quad U' = 0, \quad V' = \pm\sqrt{\sqrt{\frac{a}{b}} - 1} \tag{11}$$

4) The high confinement fixed points with non-zero zonal flow shear, when $b < a$,

$$E = \sqrt{\frac{b}{a}}, \quad V' = 0, \quad U' = \pm\sqrt{\sqrt{\frac{a}{b}} - 1} \tag{12}$$

Therefore, for a given set of parameters, there may be up to six fixed points in the high confinement regime, with a single bifurcation point for the transition from low to high confinement at $b = a$. This structure is similar to all the other models we have considered so far [7].

Having analytical solutions, it is easy to carry out the stability analysis based on the eigenvalues of the linerized equations near the fixed-point solutions. The result of this analysis shows: solutions 1) and 4) are always unstable. Solution 2) is stable and therefore is an attractor for $b > a$, and solution 3) is stable and is an attractor for $b < a$.

These solutions are giving the standard physics picture of the transition to a high confinement regime. When the damping dominates over the Reynolds stress, $b > a$, we have the low confinement solution without flow. Once the Reynolds stress dominates over the damping, shear flow is amplified and the turbulence level is reduced. In this case, we have the high confinement solution. The change of solution is continuous at the bifurcation point, but the derivative is discontinuous, the characteristic behavior of a second order transition.

At $d = 0$, the numerical results show that there are no limit cycle solutions. This will be discussed further in the next sections. When $d \neq 0$, the situation changes and becomes more complicated. As a starting point, we can only solve the equations for the fixed points numerically.

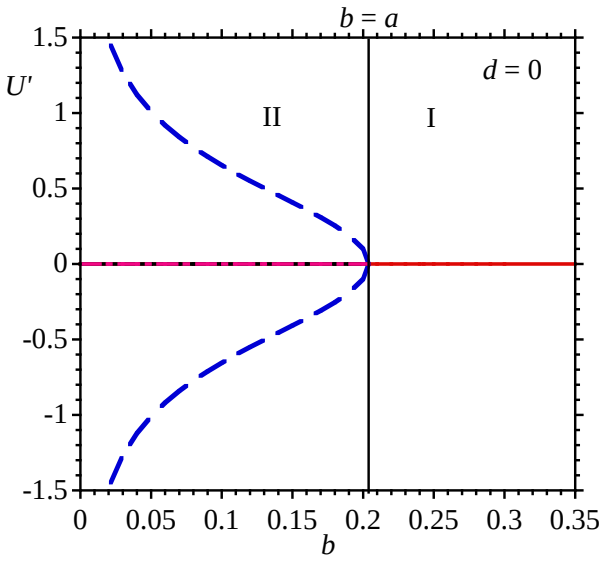

Figure 1. Fixed point solutions for U' as a function of b for $a = 0.204$, $c = 0.714$, and $d = 0$.

To show some of the complexity emerging with $d \neq 0$, we can look at some of the fixed-point solutions for U'. In Fig. 1, we plotted the fixed-point solutions for U' as a function of b. They are the same as the ones given by Eqs. (9) to (12). All stable solutions are for $U' = 0$. The bifurcation point corresponds to $b = a$ as indicated above and we have two regions, the low confinement region, further called Region I, and the high confinement region, called Region II. The transition from Region I to Region II is a second order transition.

In Fig. 2, we show the numerically calculated fixed-point solutions for U' with $d = 0.5$. We can see that a new bifurcation point for $b > a$ has appeared. If there is a transition at this bifurcation point, the transition will be a first order one. So the nature of the transition may change, but there still remains the second bifurcation point at $b = a$. After the first bifurcation, five possible fixed-point solutions exist.

The results shown in Fig. 2 only include fixed-point solutions. As we will see in the next sections, limit cycle solutions may also exist, making the potential choices of

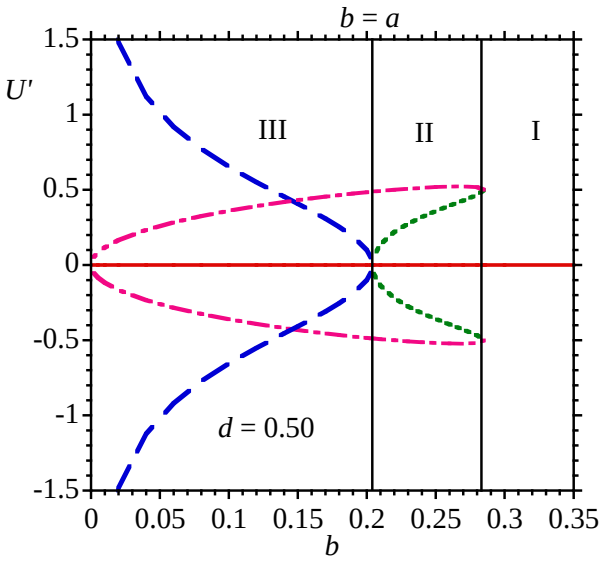

Figure 2. Fixed point solutions for U' as a function of b for $a = 0.204$, $c = 0.714$, and $d = 0.5$.

final states even more complicated. A systematic exploration of asymptotic solutions is needed in order to understand the dynamical complexity of this system of equations. This is done in the next sections.

3. Numerical exploration of the model

In order to explore the asymptotic behavior of solutions, we introduce an algorithmic method based on numerical integration of ODEs, in which we scan wide ranges of parameters and compute approximations of locally stable solutions, further called attractors for short.

We consider the phase space spanned by the variables (E, V', U'). We limit our attention to the bounded subset $B := [-0.5, 1.5]\times[-100, 100]\times[-2, 2]$ of the phase space. The subset B was chosen as a rough outer bound for all the attractors that we expect to detect, based on some preliminary computations with much larger choices of B. We take the uniform grid of $5\times5\times5$ sample points from the box $B' := [0, 1]\times[0, 10]\times[-1, 1]$. Note that due to the symmetry $(E, V', U') \mapsto (E, -V', -U')$ in the equations, we take the initial conditions with the non-negative second coordinate in order to avoid duplication of the results.

For a fixed quadruple (a, b, c, d) of parameters, we construct an approximation of all the attractors that could be reached from the sample points in the following way. We integrate each of the sample points using the Runge-Kutta method. If the iterations of the point remain in B for a certain number of steps then we plot a finite segment of the trajectory starting at the last computed iterate of the point. We plot it using 3-dimensional pixels (a.k.a. voxels) at the resolution of $8192 \times 8192 \times 8192$ in B. The family of all the topologically disjoint compact subsets of B constructed in this way are

considered to be numerical approximations of the attractors.

For each of the constructed sets, we compute its Betti numbers $(\beta_0, \beta_1, \beta_2)$ in order to determine its basic topological properties. Here β_0 counts the number of connected components, β_1 counts the number of tunnels (or through-holes), and β_2 counts the number of voids. In particular, the Betti numbers $(1, 0, 0)$ suggest a fixed point, and the Betti numbers $(1, 1, 0)$ indicate a circle-shaped set, probably a periodic orbit for the underlying ODE.

In order to obtain a comprehensive picture of the asymptotic dynamics over a wide range of parameters, we fix $c := 0.714$ and $d \in [0, 1]$, and we run the above-described computations for all the endpoints (a, b) of a uniform grid of 1000×1000 intervals into which we subdivide the parameter space $P := [0, 1]^2$ being scanned. These computations were run at a computer cluster using the distributed computations scheme introduced in Ref. [16].

In Fig. 3, we show the results obtained with this method for a few selected values of d. Regions that differ by the number or type of attractors found are labeled and discussed below. Since the most interesting part of the picture is for the values of $(a, b) \in [0, 0.4]^2$, we limit the presentation of results to these values of the parameters, or otherwise some regions in the images become too small to be clearly distinguished. The way in which the shape of the attracting cycle changes with varying b is illustrated in Fig. 4.

In Region (a), where the damping dominates over the Reynolds-Maxwell terms, there is only one fixed-point attractor, the low confinement fixed point without shear flows. This fixed point becomes unstable, no longer an attractor, at the line $a = b$, which is clearly visible in all the graphs in Fig. 3. This line limits Region (b), in which two attractors are present, the low and the high confinement fixed points. The line separating Regions (a) and (b) is the line of bifurcation points where the high confinement fixed point emerges, and corresponds to the point separating Regions I and II in Fig. 2.

For values of a and b close to 1, Region (b) becomes very narrow and the emergence of the high confinement fixed point and the destabilization of the low confinement fixed point are nearly simultaneous. For these values of a and b the situation is similar to the case $d = 0$ and the transition to the high confinement is similar to a second order transition. In Region (c), there is only one attractor: the high confinement fixed point.

An interesting situation can be seen in Regions (d) and (e), where an attracting limit cycle was found. This solution depends strongly on the value of d and does not exist for $d = 0$. The limit cycle solution is practically independent of the value of a. As d increases, the value of b at which the limit cycle appears also increases. In Region (d), the limit cycle solution coexists with the low confinement fixed-point attractor.

As we move to Regions (f) and (g), the limit cycle solution is no longer found. It is not clear if this solution no longer exists or there is a numerical problem in finding it. In Fig. 4, we plotted the projection of the limit cycle solution on the (V', E) plane. One can see that as the parameter b decreases, the cycle becomes larger and larger, and also gets closer to the axes $E = 0$ and $V' = 0$. In this situation, small errors can make

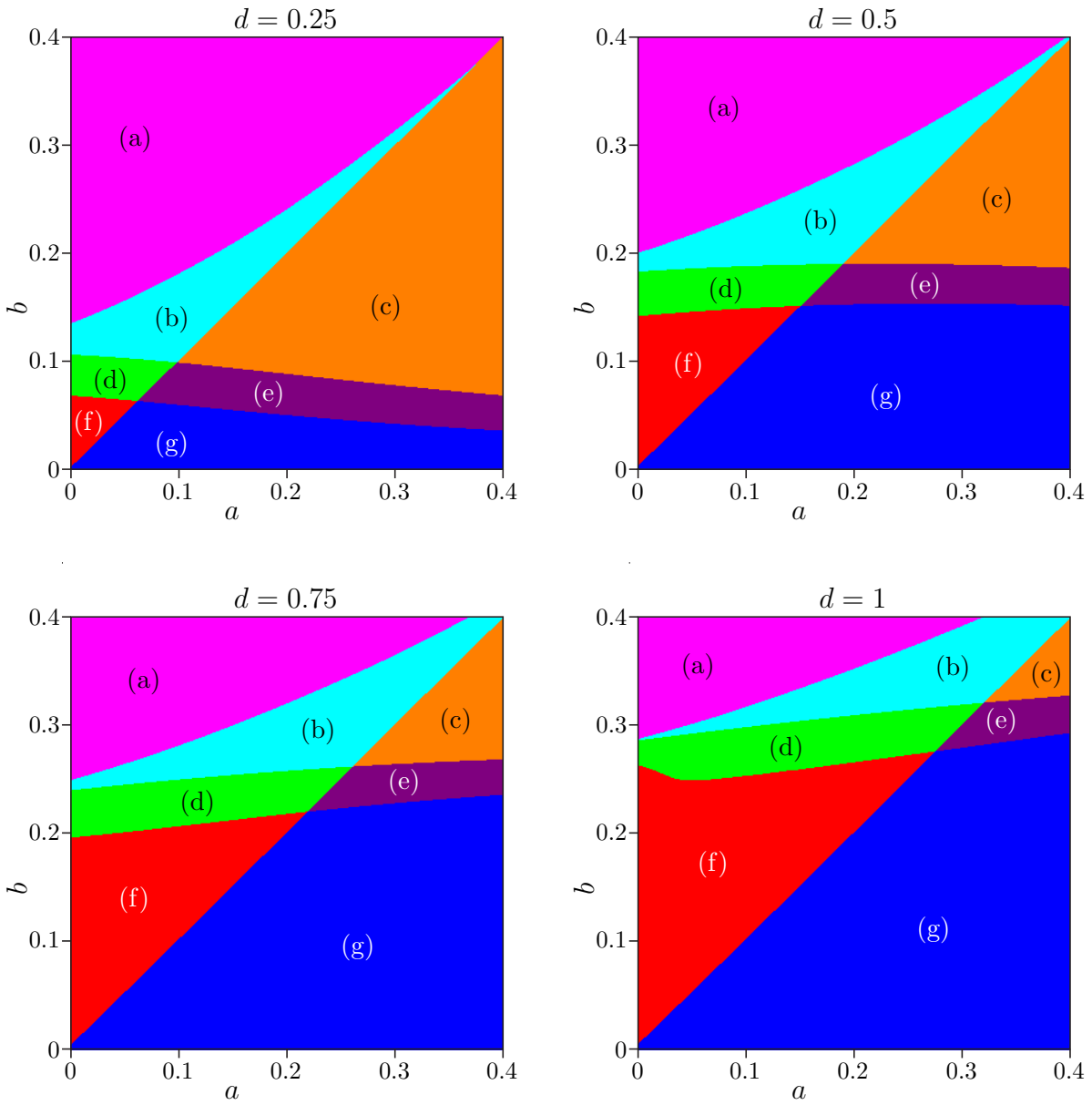

Figure 3. Regions with different numbers or types of attractors found with the numerical method discussed in Section 3, as a function of a and b for $c = 0.714$ and a few selected values of d. The numbers of attractors found are as follows: Two in (b), (d), one in (a), (c), (e), (f), none in (g). An attracting cycle was found in (d) and (e).

it impossible to identify the solution. The limit cycle solutions have a full 3D structure in the phase space, as shown in Fig. 5.

In Region (f), there exists only one attractor, the low confinement fixed point. In Region (g), no attractors were found.

Because of the structure of the solutions, several ways of transitioning to high confinement are possible. Let us assume that both a and d are fixed, with $d = 0.5$, and we are decreasing the parameter b. If $a > 0.2$, one may have a transition to the high confinement fixed point as it emerges or when the low confinement fixed point becomes

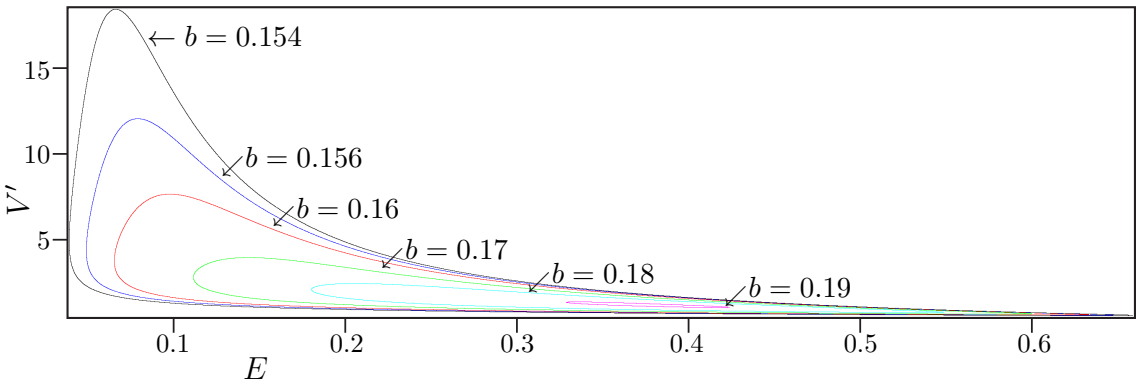

Figure 4. A projection to the (E, V') plane of the attracting cycle found for $a = 0.204$, $c = 0.714$, and $d = 0.5$, at a few different values of b.

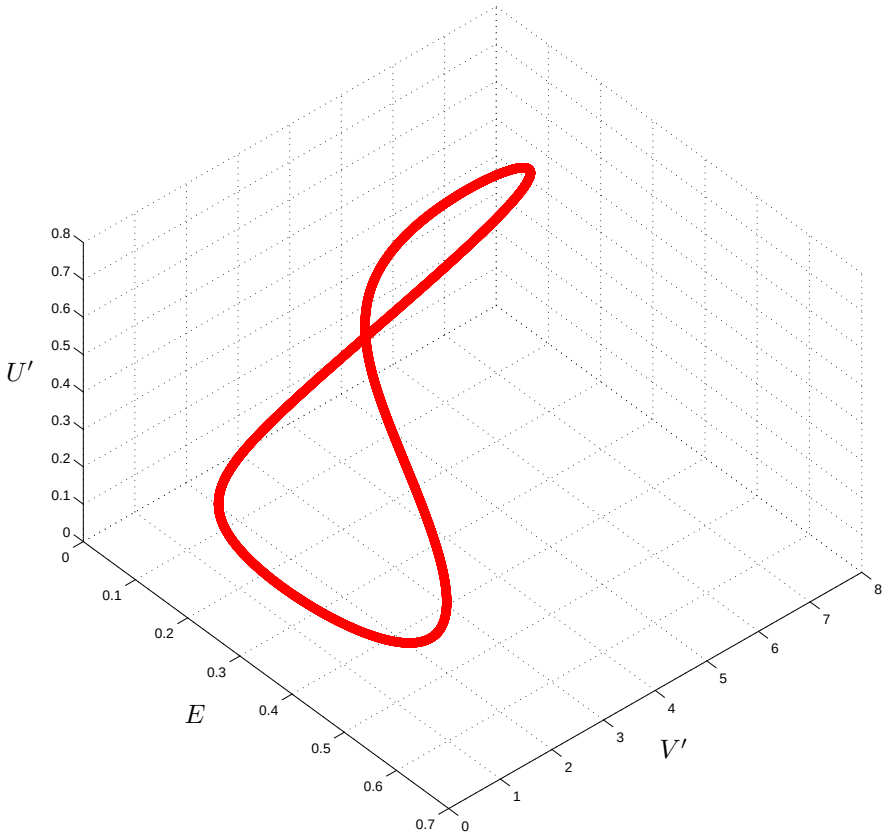

Figure 5. Limit cycle solution in the phase space for $a = 0.204$, $b = 0.16$, $c = 0.714$, and $d = 0.5$.

unstable at $b = a$. However, for $a < 0.2$ it may transition first to the limit cycle before going in the high confinement fixed point.

4. Topological-combinatorial computations

In order to conduct a more in-depth analysis of the dynamics, not only limited to stable invariant sets but also taking the unstable ones into consideration, we analyze the global dynamics of the system using the software introduced in [1].

The idea behind this approach is to decompose the phase space into recurrent components (fixed points, periodic orbits, etc.) such that the connecting orbits between them define a strict partial order, like in a gradient flow. This is achieved by computing an outer approximation of a Morse decomposition at a prescribed resolution, consisting of isolating neighborhoods of Morse sets, further called combinatorial Morse sets for short. The interested reader is referred to [1] and to references therein for a detailed explanation of this method and for the corresponding software.

The computational method is designed for maps, so we work with a time-t discretization (for $t = 2$) of the flow induced by the system (6)-(8). We use the CAPD software (`http://capd.ii.uj.edu.pl/`) for rigorous integration of the flow, which is quite time-consuming and produces considerable overestimates, but gives mathematically rigorous results. However, instead of constructing isolating neighborhoods valid for entire subintervals of parameters (which is usually done when using this method), we plug in individual parameter values in order to minimize the overestimates.

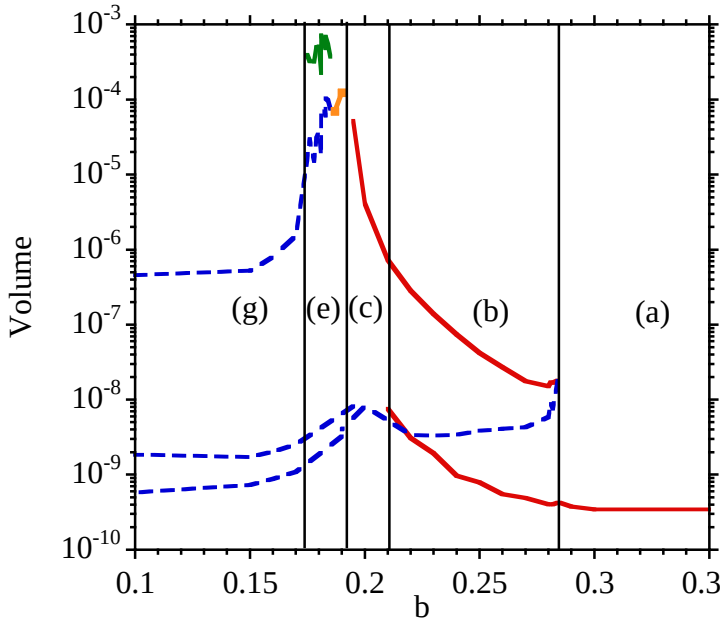

Figure 6. Volume of the combinatorial Morse sets, normalized to the volume of a fixed bounding box in the phase space, as a function of b for $a = 0.204$, $c = 0.714$, and $d = 0.5$. In this figure, continuous lines correspond to attractors.

We have done many scans with one varying parameter in order to explore in more detail the properties of this dynamical system. Here we show one example of these scans. In Fig. 6, we plotted the volume of the combinatorial Morse sets found by the method normalized to the volume of a fixed phase space bounding box in which we conducted the computations. The results are for $a = 0.204$ and $d = 0.5$. In the corresponding plot in Fig. 3, this scan is a vertical path for $a = 0.204$. One can see that this path goes through Regions (a), (b), (c), (e) and (g), as indicated in the figure. This scan also corresponds to the calculation of fixed points in Fig. 2. There, Region I corresponds to Region (a), II to (b), and III includes (c), (e) and (g). In Fig. 6, attractors are indicated by continuous lines.

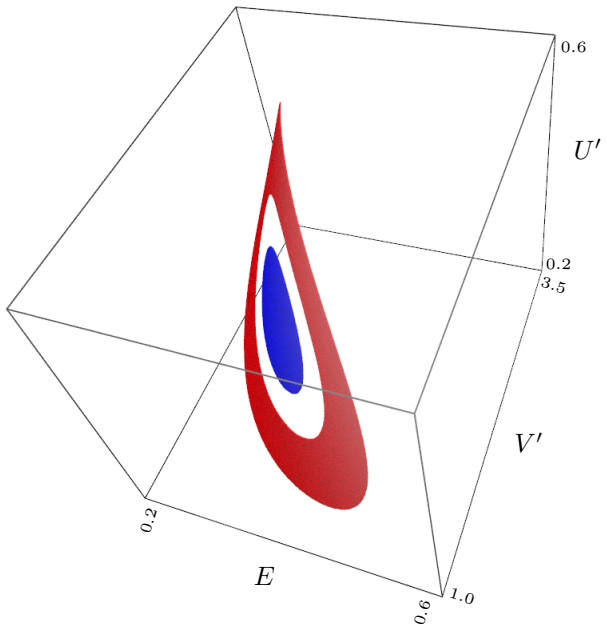

Figure 7. Isolating neighborhoods of the unstable high confinement fixed point and of the limit cycle constructed for $b = 0.185$ in the scan that is a basis for the data illustrated in Fig. 6. (Brighter part of the neighborhood is closer to the viewer.)

As mentioned before, the calculation overestimates the size of the Morse sets. This is particularly obvious in the transition from Region (c) to (e), where an attractor fixed point solution, the high confinement fixed point, bifurcates in a fixed point and a limit cycle. Fig. 7 shows combinatorial Morse sets containing the high confinement fixed point and the limit cycle for $b = 0.185$, which is close to the bifurcation point. Fig. 8 shows the corresponding two combinatorial Morse sets for a somewhat lower value of b, namely, $b = 0.179$.

The properties of each of the Morse sets are reflected by the Conley index [9], a generalization of the Morse index of a nondegenerate critical point of a flow that carries information about how the flow behaves near that set. For the computations we use the homological version for discrete-time dynamical systems [15, 17]. Roughly speaking, the Conley index of an invariant set consists of the relative homology groups of an

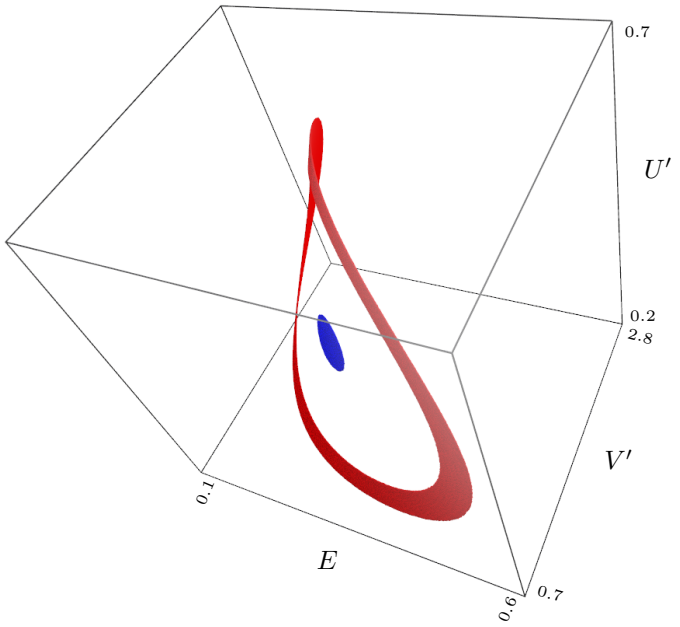

Figure 8. Isolating neighborhoods of the unstable high confinement fixed point and of the limit cycle constructed for $b = 0.179$ in the scan that is a basis for the data illustrated in Fig. 6. (Brighter part of the neighborhood is closer to the viewer.)

isolating neighborhood of the invariant set and the part of its forward image that sticks out of the isolating neighborhood, called its *exit set*, together with a certain class of automorphisms on these groups that in our case are just the identity maps, since we work with a time-t map of a flow.

Consider two extreme types of Morse sets. One is the case of an attractor. In this case, the exit set is empty and the Conley index reflects the topological properties of the isolating neighborhood of the attractor. The other extreme is a fixed point. In this case, the Conley index reflects the topological properties of the exit set, and corresponds to the dimension of the unstable manifold of the fixed point.

Let us now explain the meaning of the indices we encountered in the parameter scan described above. The Conley index (H_0, H_1, H_2, H_3) for each of the different Morse sets in Fig. 6 is listed in Table 4. The combinatorial Morse sets have been numbered from the largest to the smallest volume.

$H_0 = \mathbb{Z}$ suggests that the exit set is empty, i.e., the invariant set is an attractor. In particular, $(\mathbb{Z}, 0, 0, 0)$ in the Conley index of an attracting fixed point, and $(\mathbb{Z}, \mathbb{Z}, 0, 0)$ suggest a limit cycle. The index $(0, \mathbb{Z}, 0, 0)$ suggests a fixed point with a 1-dimensional unstable manifold, and the index $(0, 0, \mathbb{Z}, 0)$ — with a 2-dimensional unstable manifold.

5. Conclusions

In the dynamical model describing the coupling of turbulence and average flow, the inclusion of zonal flows has increased significantly the complexity of the model and the number of potential types of transitions.

Region	Morse set	Conley index
(a)	1	$(\mathbb{Z}, 0, 0, 0)$
(b)	1	$(\mathbb{Z}, 0, 0, 0)$
	2	$(0, \mathbb{Z}, 0, 0)$
	3	$(\mathbb{Z}, 0, 0, 0)$
(c)	1	$(\mathbb{Z}, 0, 0, 0)$
	2	$(0, \mathbb{Z}, 0, 0)$
(e)	1	$(\mathbb{Z}, \mathbb{Z}, 0, 0)$
	2	$(0, 0, \mathbb{Z}, 0)$
	3	$(0, 0, \mathbb{Z}, 0)$
	4	$(0, \mathbb{Z}, 0, 0)$
(g)	1	$(0, 0, \mathbb{Z}, 0)$
	2	$(0, 0, \mathbb{Z}, 0)$
	3	$(0, \mathbb{Z}, 0, 0)$

Table 1. Conley indices of the combinatorial Morse sets indicated in Fig. 6, ordered decreasingly by their volume.

The topological analysis of the Morse sets for this dynamical model has proven to be very effective in the determination of the stability properties of non-fixed-point asymptotic solutions for which the approach of linearizing the dynamical equations in their neighborhood cannot be applied. This allowed us to deal with the complexity of the model in a better way.

The systematic exploration of the asymptotic solutions of this three-equation model has shown that depending on the relative effective contributions of the Reynolds-Maxwell terms and of the damping term, the transition to a high confinement regime may vary from a second order type transition to a first order transition or to dithering transitions.

In the case of the stellarator plasma edge where the damping is large, the transition leading to the formation of the shear flow layer is more similar to a second order transition. For high temperature tokamaks, the H-mode type transition will be like a first order transition, but dithering transitions may exist. A more detailed quantitative determination of the Reynolds-Maxwell terms will be necessary in the determination of which is the most likely one.

Acknowledgments

This research was sponsored in part by DGICYT (Dirección General de Investigaciones Científicas y Tecnológicas) of Spain under Project No. ENE2009-12213-C03-03. Additionally, PP acknowledges the support obtained from Departamento de Física of Universidad Carlos III de Madrid, and also from Fundo Europeu de Desenvolvimento Regional (FEDER) through COMPETE—Programa Operacional

Factores de Competitividade (POFC) and from the Portuguese National Funds through Fundação para a Ciência e a Tecnologia (FCT) in the framework of the research projects FCOMP-01-0124-FEDER-010645 (ref. FCT PTDC/MAT/098871/2008) and Est-C/MAT/UI0013/2011.

Moreover, the authors thank the Computer Science and Technology Center at Departamento de Informática of Universidade do Minho, and also K. Mischaikow's lab (the latter supported in part by NSF, DoE, DARPA, and AFOSR) at Rutgers University for providing their cluster computing facilities.

References

[1] Arai Z, Kalies W, Kokubu H, Mischaikow K, Oka H and Pilarczyk P 2009 A database schema for the analysis of global dynamics of multiparameter systems, *SIAM J. Appl. Dyn. Syst.* **8** 757–789

[2] Biglari H, Diamond P H and Terry P W 1990 Influence of sheared poloidal rotation on edge turbulence, *Phys. Fluids B* **2**, 1–4

[3] Burrell K H 1997 Effects of $E \times B$ velocity shear and magnetic shear on turbulence and transport in magnetic confinement devices, *Phys. Plasmas* **4** 1499–1518

[4] Calvo I, Carreras B A, Garcia L, Pedrosa M A and Hidalgo C 2009 Zonal flows and long-distance correlations during the formation of the edge shear layer in the TJ-II stellarator, *Plasma Phys. Control. Fusion* **51** 065007

[5] Carreras B A, Lynch V E and Garcia L 1991 Electron diamagnetic effects on the resistive pressure-gradient-driven turbulence and poloidal flow generation, *Phys. Fluids B* **3** 1438–1444

[6] Carreras B A, Newman D, Diamond P H and Liang Y-M 1994 Dynamics of low to high ("L" to "H") confinement bifurcation: Poloidal flow and ion pressure gradient evolution, *Phys. Plasmas* **1** 4014–4021

[7] Carreras B A, Garcia L, Pedrosa M A and Hidalgo C 2006 Critical transition for the edge shear layer formation: Comparison of model and experiment *Phys. Plasmas* **13** 122509

[8] Colchin R J, et al 2002 Slow L-H transitions on DIII-D, *Phys. Rev. Lett.* **88** 255002-1

[9] Conley C 1978 *Isolated invariant sets and the Morse index* (Providence, RI: Amer. Math. Soc.)

[10] Diamond P H and Kim Y B 1991 Theory of mean poloidal flow generation by turbulence, *Phys. Fluids B* **3** 1626–1633

[11] Diamond P H, Liang Y-M, Carreras B A and Terry P W 1994 Self-Regulating Shear Flow Turbulence: A Paradigm for the L to H Transition, *Phys. Rev. Lett.* **72** 2565–2568

[12] Diamond P H, Itoh S-I, Itoh K and Hahm T S 2005 Zonal flows in plasma—a review, *Plasma Phys. Control. Fusion* **47** R35

[13] Hasegawa A and Wakatani M 1987 Self-organization of electrostatic turbulence in a cylindrical plasma, *Phys. Rev. Lett.* **59** 1581-1584

[14] Kim E and Diamond P H 2003 Zonal Flows and Transient Dynamics of the L-H Transition, *Phys. Rev. Lett.* **90** 185006

[15] Szymczak A 1995 The Conley index for discrete semidynamical systems, *Topology Appl.* **66** 215–240

[16] Pilarczyk P 2010 Parallelization method for a continuous property, *Found. Comput. Math.* **10** 93–114

[17] Pilarczyk P and Stolot K 2008 Excision-preserving cubical approach to the algorithmic computation of the discrete Conley index *Topology Appl.* **155** 1149–1162

[18] Terry P W 2000 Suppression of turbulence and transport by sheared flow, *Rev. Mod. Phys.* **72** 109–165

[19] Wagner F *et al.* 1982 Regime of Improved Confinement and High Beta in Neutral-Beam-Heated Divertor Discharges of the ASDEX Tokamak, *Phys. Rev. Letters* **49** 1408–1412